



# Dynamic electric behavior and open-circuit-voltage modeling of LiFePO<sub>4</sub>-based lithium ion secondary batteries

Michael A. Roscher\*, Dirk Uwe Sauer

RWTH Aachen University, Electrochemical Energy Conversion and Storage Systems Group, Institute for Power, Electronics and Electrical Drives (ISEA), Jaegerstrasse 17-19, 52066 Aachen, Germany

## ARTICLE INFO

### Article history:

Received 19 April 2010

Received in revised form 28 June 2010

Accepted 30 June 2010

Available online 7 July 2010

### Keywords:

Li-ion

Battery modeling

LiFePO<sub>4</sub> cathode

OCV hysteresis

## ABSTRACT

Accurate battery modeling is one of the key factors in battery system design process and operation as well. Therefore, the knowledge of the distinct electric characteristics of the battery cells is mandatory. This work gives insight to the electric characteristics of lithium ion batteries (Li-ion) comprising LiFePO<sub>4</sub>-based cathode active materials with emphasis on their specific open-circuit-voltage (OCV) characteristics including hysteresis and special OCV recovery effects, which last for several minutes or even hours after a current load is interrupted. These effects are elucidated incorporating OCV measurement data of high power cells. Simple empiric models are derived and used in a model-based state estimation algorithm. The complete battery model includes an impedance model, a hysteresis model and an OCV recovery model part. The introduced model enables the assessment of the cells' state-of-charge (SOC) precisely using model-based state estimation approaches.

© 2010 Elsevier B.V. All rights reserved.

## 1. Introduction

Storing electric energy effectively is one of the most challenging issues for many portable high electric power and energy consuming applications. For battery electric vehicles (BEV) and hybrid electric vehicles (HEV) the lithium ion technology (Li-ion) is currently the best trade off between energy and power density on one hand and the costs of a storage system on the other hand side. In the course of recent research and development in the field of Li-ion batteries the iron-based olivine type cathodes (mainly lithium iron phosphate, LiFePO<sub>4</sub>) were identified as promising alternatives to cathodes based on rare metal composites (i.e. the transition metal oxides LiCoO<sub>2</sub>, LiNiO<sub>2</sub>) in terms of power density and cycle life time [1,2]. These olivine typed cathode materials are environmental benign (nontoxic) and therefore have found the way to lower-cost large scale energy storage systems, due to the involved materials being accessible in high quantities.

Besides the stated advantageous properties the LiFePO<sub>4</sub>-batteries show some detrimental aspects in comparison to the rare metal-based cathode chemistries. One drawback refers to the lower energy density caused by the reduced operating voltage of the LiFePO<sub>4</sub> cells in a range of  $U_{\text{cell}} = 2.5\text{--}3.6\text{ V}$  (compared to  $3\text{--}4.2\text{ V}$  of LiCoO<sub>2</sub> cells [3]). Additionally, the cells' open-circuit-voltage (OCV) characteristics include very flat OCV curves over the state-

of-charge (SOC) and exhibit pronounced hysteresis phenomena, as another critical aspect. These very special OCV characteristics complicate the estimation of a battery's state-of-charge and therefore the determination of mandatory information for a reliable operation, i.e. energy content and instantaneous power capability.

In the following sections the need for precise battery modeling is elucidated. Important aspects characterizing the electrical behavior of LiFePO<sub>4</sub>-based Li-ion cells will be outlined and adequate model approaches will be presented, which enable the reconstruction of the specific OCV characteristics. Thereafter, the developed battery model, which includes the special OCV effects of the selected cathode material, is demonstrated and validated.

## 2. Top-down battery modeling

The reconstruction of the battery's electric behavior is relevant for the system design process as well as for reliable battery operation. During system designing battery models are used to simulate typical operation conditions. Therefore, the required energy and power contents of the storage system, which determine the required number and type of the battery cells can be derived. Furthermore, the cooling requirements can be investigated for specific cell assemblies and battery system housings.

On the other hand side, the battery modeling is mandatory for reliable battery management. Model-based state estimation algorithms enable the assessment of crucial battery information, i.e. critical temperatures, state-of-charge (SOC) or state-of-health (SOH). For Li-ion batteries' state estimation various model-based

\* Corresponding author. Tel.: +49 89 38211380; fax: +49 89 3827011380.  
E-mail address: [michael.roscher@rwth-aachen.de](mailto:michael.roscher@rwth-aachen.de) (M.A. Roscher).

algorithms are documented in the literature (i.e. adaptive filters [4,5], Kalman-Filters [6,7], extended Kalman-Filters [8,9], and sliding mode observers [10]). The referenced methods use simple battery models to reproduce the batteries' electrical behavior. The models include lumped electrical equivalent circuits comprising resistors and capacitors (e.g. Randles equivalent circuit [11]) to reproduce the transient battery voltage responses on current load. In addition to the electric equivalent circuits the batteries' open-circuit-voltage (OCV) is reproduced by empiric or analytic expressions of the OCV depending on the temperature and SOC, in some cases superimposed by hysteresis effects [9].

For reliable state estimation high precise models are required to access the battery state information accurately. In the following sections the model development and model parameterization are outlined for high power Li-ion cells based on  $\text{LiFePO}_4$  active cathode material (graphite based anode). Considering the results obtained from electrical cell characterization tests a dynamic battery model, an OCV model approach, and a hysteresis model are derived.

### 3. Experimental

The electrical tests are divided in two separated test schedules, a parameterization and a validation test schedule.

#### 3.1. Model design and parameterization tests

The model parameterization test schedule includes pulse current tests and OCV tests. In a first test the dynamic electric cell behavior under load is investigated. Therefore, charge and subsequent discharge current pulses (each lasting 20 s) are applied to the cells. The described pulse load test is carried out with various current rates (1C, 5C, 20C) starting at SOC = 20%, 40%, 60%, and 80%. Prior to each pulse the cells are fully charged (SOC = 100%) with a CCCV load regime (constant current (1C) until 3.6 V; constant voltage 3.6 V for 30 min). After the distinct initial SOC is adjusted through discharge and the cells are resting for 30 min the constant current pulses are applied.

During the first OCV test (boundary curve test) the cells are gradually discharged (in 5%  $\Delta$ SOC steps beginning at SOC = 100% (CCCV), with constant current 0.5C) until the discharge cutoff voltage (2 V) is reached. Then the cells are recharged again (5% steps, 0.5C). At each SOC step the cells are in the open circuit condition for 3 h.

In a second OCV test the hysteresis effects are investigated. Therefore, gradual partial cycles are applied to achieve the intermediated OCV curves between the OCV boundary curves. At first the cells (SOC = 100%) are discharged to SOC = 69%. After 3 h rest the cells are charged by  $\Delta$ SOC = 2% for six times ( $\rightarrow$  SOC = 81% with 0.5C; including 3 h rest periods). Then the cells are discharged again in six steps (2% steps, 0.5C). The same cycle is repeated for initial SOC = 44% and 19%, respectively. To investigate the OCV behavior after charging the completely discharged cells (the nominal capacity  $C_{\text{nom}}$  is extracted from the cells being CCCV charged previously) are charged to SOC = 31% (0.5C). Then the cells are discharged gradually to SOC = 19% (6 steps with  $\Delta$ SOC = 2%,  $I = 0.5C$ , 3 h rest included) and the cells are stepwise charged to SOC = 31% again. The same test cycle is repeated for initial SOC = 56% and 81%, respectively.

#### 3.2. Validation test

In order to validate the battery model a typical HEV load cycle is applied to the cells. Herein, a current sequence derived from the New European Drive Cycle (NEDC) through simulations of an HEV prototype is used as an example. This load cycle is very dynamic with current peaks of more than 20C and operates in the mid SOC range, which is a typical battery use case in HEV applications. One

NEDC cycle takes approximately 20 min. The entire validation test includes ten NEDC cycles with rest periods of 5 min in-between the distinct cycles. The cell current and voltage are measured at constant time intervals for  $T = 10$  ms during testing. At the beginning the cells are fully charged (CCCV). Then the cells are discharged to the initial point of SOC = 70% and rested for 30 min before the test cycle is applied.

The battery model's correctness in simulating the real battery electric behavior is validated by comparing the measured and the modeled voltage response on the applied current sequence. Therefore, the battery model is implemented in a linear state observer structure. The obtained sequences of current and voltage during NEDC cycling are incorporated as input data for the state observer in the Matlab/Simulink development environment. If the voltage reconstruction proceeds accurately the state observer explores the battery's SOC. With this procedure the model's accuracy can generally be validated. Additionally, the usability of the developed and parameterized model for reliable state-of-charge estimation can be demonstrated.

#### 3.3. Measurement equipment

The cell characterization and validation test are carried out on single cells. The OCV boundary curve tests are done on a Digatron test bench (0, ..., 5 V,  $\pm 50$  A) that comprises a voltage measurement accuracy of  $\pm 1$  mV and a current measurement accuracy  $\pm 0.1\%$  (of the full scale value). The pulse tests, the hysteresis tests and the validation tests are carried out on a Scienlab test bench ( $\pm 60$  V,  $\pm 300$  A, measurement accuracy:  $\pm 0.25\%$  of the measured voltage  $\pm 1$  mV and  $\pm 0.25\%$  of the measured current  $\pm 30$  mA in a range of  $-30$  A to  $+30$  A and  $\pm 0.25\%$  of the measured value  $\pm 600$  mA for higher currents, respectively).

During testing the cells are located in CTS climate chambers and the cells ambient temperatures are constantly held at 25 °C.

### 4. Results, model identification and verification

First of all, the obtained results are used to achieve and parameterize an appropriate battery model that incorporates dynamic and open-circuit-voltage effects. Subsequently the model is used to reconstruct the real cell behavior during typical battery operation.

#### 4.1. Dynamic battery model

A typical voltage response of the investigated cells at SOC = 40% on a charge pulse (constant current 20C) is given in Fig. 1a. The cell voltage comprises a straight-way and a transient fraction, superposed by the cell's OCV.

The straight-way fraction is caused by the resistive components of the cells, i.e. terminals, tabs, collector foils, bulk materials, electrolyte [12]. The transient voltage drop results from diffusion and charge transportation processes as well as effects being related to the electric double layer capacitance at the interface between electrolyte and active materials [13]. An ohmic-transient voltage response behavior, as given in Fig. 1a, can be similarly observed for all SOC values (SOC = 20%, 40%, 60%, and 80%) during charge and discharge pulses. This dynamic electric behavior can be reconstructed using an equivalent circuit model consisting of a resistor  $R_s$  connected in series to a parallel branch of a resistor  $R_p$  and a capacitor  $C_p$ . Such an equivalent circuit is widely used (e.g. [14]) and is also depicted in Fig. 1b (with the OCV being included as a voltage source). Thus, the instantaneous cell voltage  $U_{\text{cell}}$  is a function of OCV and the cell current  $I_{\text{cell}}$ . An analytic expression of  $U_{\text{cell}}$  in the frequency domain is given in Eq. (1), where  $\omega$  is the angular

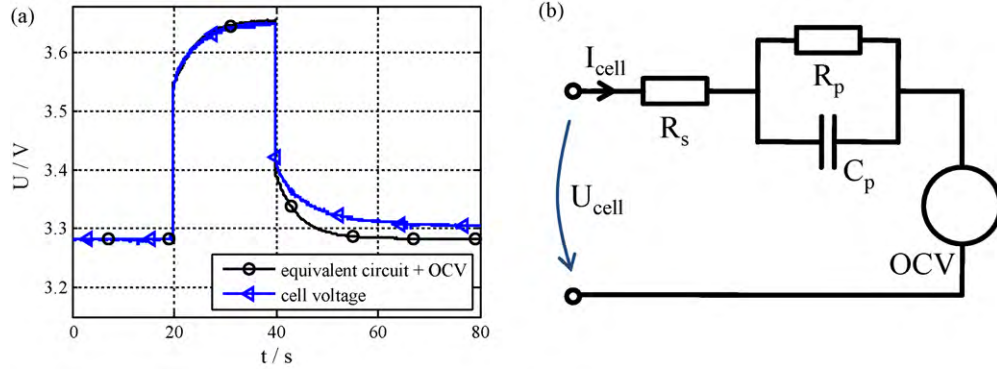


**Fig. 1.** Voltage response on a 20C constant current charge pulse (a) and the preferred battery electric equivalent circuit for voltage reconstruction (b).

frequency of the current excitation.

$$U_{\text{cell}}(j\omega) = I_{\text{cell}}(j\omega) \cdot \left( R_s + \frac{R_p}{1 + j\omega R_p C_p} \right) + \text{OCV} \quad (1)$$

The simulated voltage response on the constant current pulse using the illustrated equivalent circuit is given in Fig. 1a. By fitting the components  $R_s$ ,  $R_p$ ,  $C_p$  of the equivalent circuit, the voltage can be reproduced accurately. With the simple RRC-model the maximum deviation between the modeled and the measured voltage is less than 4 mV during the applied 20C pulse. During the current pulse the OCV changes, due to the changing SOC. The OCV drift leads to the difference between the measured cell voltage and the voltage of the battery model (where the OCV is held constant) for  $t > 40$  s in Fig. 1a.

#### 4.2. OCV model development and parameterization

The gradual complete discharge and subsequent charge cycles emphasize the pronounced OCV hysteresis of the investigated cells. This is expected since it is known that  $\text{LiFePO}_4$  [15] and graphite [16] exhibit pronounced OCV hysteresis phenomena. Hence, the OCV after previous charge is higher than the OCV after discharge at the same SOC value, which is illustrated in Fig. 2. Accordingly, two different OCV curves exist,  $\text{OCV}_{\text{charge}}$  and  $\text{OCV}_{\text{discharge}}$ , describing the specific OCV characteristics of the investigated cells.

Both of the curves comprise characteristic OCV plateaus. The gap between the two curves depends on the SOC and exhibits local minima at SOC = 40% and 85% and local maxima at SOC = 20% and 65% and reaches a maximum value of approximately 60 mV. For OCV

model development both of the curves ( $\text{OCV}_{\text{charge}}$  and  $\text{OCV}_{\text{discharge}}$ ) will be considered.

In Fig. 2 the measured OCV values after 1 min, 5 min and 30 min rest time are inserted additionally. These intermediate values indicate that the OCV recovers over several minutes and even hours until a steady state is reached. (The OCV changes less than 1 mV from 3 h to 8 h rest and hence is assumed to be stable.) Moreover, the voltage decay depends on the SOC. The characteristic plateaus cannot be identified clearly after 1 min rest; they rather emerge during rest. The OCV recovery is depicted in Fig. 3, plotted over SOC, where the differences between the measured OCVs after certain rest durations and the OCV curves after 3 h rest, which are assumed to be almost stable, are given.

The cell voltage recovery over several minutes or hours cannot be reproduced with the simple equivalent circuit model as it is given in Fig. 1b, comprising a resistor  $R_s$  connected in series with a parallel RC branch ( $R_p$ ,  $C_p$ ). The OCV decay effect has to be considered separately. A possible way to incorporate the information about the rest time for OCV reproduction is to introduce a recovery factor  $\lambda$ , which indicates whether the OCV is completely recovered (to its values after 3 h rest) or not. During load the recovery factor is equal to  $\lambda = 1$  and  $\lambda = 0$  if the OCV is in a steady state after 3 h rest. Therefore, the transition from  $\lambda = 1$  to  $\lambda = 0$  during rest periods is assumed to proceed as first order exponential decay, according to Eq. (2), with the time constant of the OCV decay  $\tau$ .

$$\lambda(t_{\text{rest}}) = \exp\left(\frac{-t_{\text{rest}}}{\tau}\right) \quad (2)$$

The cell voltage values at the beginning ( $t_{\text{rest}} \rightarrow 0$ ) of the distinct rest periods as well as after very long rest periods ( $t_{\text{rest}} \rightarrow \infty$ ) are

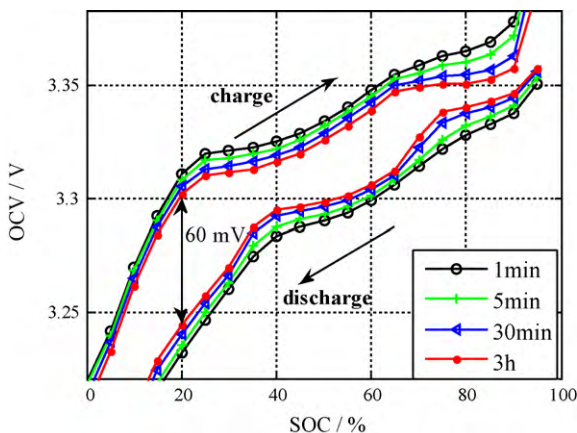


**Fig. 2.** OCV curves of the  $\text{LiFePO}_4$ -based cells depending on the previous current direction, measured after various rest periods at each step.

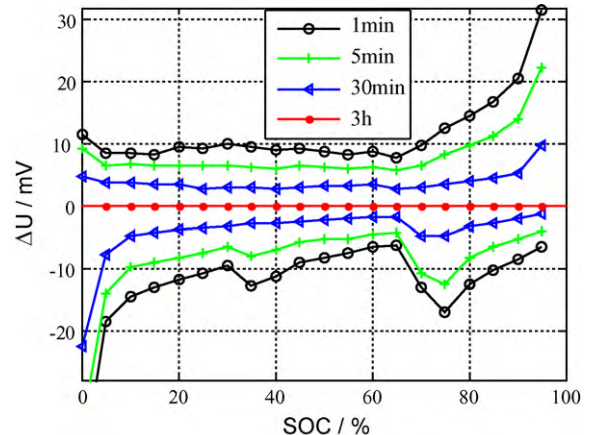


**Fig. 3.** Voltage recovery during gradual OCV testing for various rest durations plotted over SOC, with the OCV after 3 h used as reference.



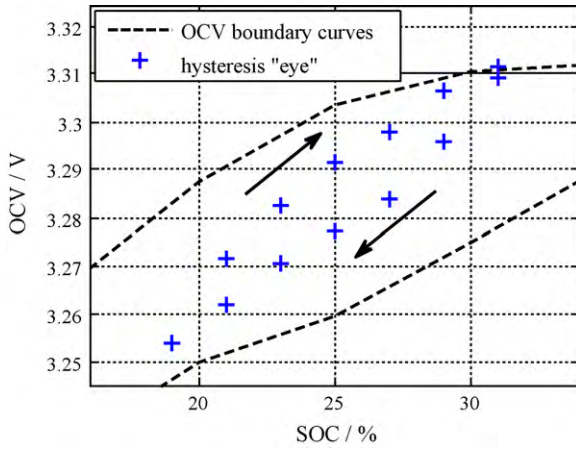


**Fig. 4.** Complete gradual OCV test cycle starting on the  $OCV_{charge}$  boundary curve at  $SOC = 31\%$  (→ centered at  $SOC = 25\%$ ).

to be considered for the accurate reconstruction of the cells' OCV recovery. The  $t_{rest} \rightarrow \infty$  condition is nearly met for the OCV values measured after 3 h rest. The OCV at the beginning of the rest periods cannot be directly accessed owing to the superimposed voltage drop caused by the load in the internal cell impedance, as stated above. We suggest including the measured voltages after 1 min rest instead, as we assume that the impedance based voltage drop has vanished and the OCV recovery remains only. Therefore, OCV curves after  $t_{rest} = 1$  min are treated as  $OCV_{1min}$  and after 3 h as stable  $OCV_{3h}$ , respectively. The recovery factor  $\lambda$  determines the weighting of both of the curves, according to Eq. (3), which is appropriate for the  $OCV_{charge}$  and the  $OCV_{discharge}$  as well. This implies that the (virtual) OCV during load is equal to  $OCV_{1min}$ .

$$OCV(SOC, \lambda) = \lambda \cdot OCV_{1min}(SOC) + (1 - \lambda) \cdot OCV_{3h}(SOC) \quad (3)$$

Beyond regarding the OCV values after the cells are monotonously discharged or charged, the OCV after intermittent, alternating load scenario is also to be reconstructed for accurate battery modeling. This is methodically investigated by applying gradual partial cycles to the cells to investigate how the OCV transits between the OCV boundary curves ( $OCV_{charge}$  to  $OCV_{discharge}$  and vice versa) as a consequence of non-monotone loading. The partial cycles start on one of the OCV boundary curves and comprise a charge throughput of 24% of the nominal Ah-capacity  $C_{nom}$  (6 charge steps with  $\Delta SOC = 2\%$  and 6 discharge steps, respectively). Fig. 4 illustrates the measured OCV values (after 3 h rest) during one downward cycle (centered at an  $SOC = 25\%$ ), with discharge steps beginning at  $SOC = 31\%$  on the  $OCV_{charge}$  curve and subsequent charge steps. As visible in Fig. 4, the measurable OCV values enclose a complete hysteresis "eye", similarly to those documented for nickel metal hydride batteries, e.g. in [17]. Noticeably, the OCV values do not reach the contrarian OCV boundary curve completely, even if the charge throughput is higher than  $10\% C_{nom}$ . This is indicated for upward cycles (starting on  $OCV_{discharge}$ ) and downward cycles (starting on  $OCV_{charge}$ ), respectively, for all of the three initial SOC values.

However, to empirically reconstruct the transition between the boundary curves a simple hysteresis model is introduced. The model's input is the battery current and its output is the hysteresis factor  $\Psi$ . The factor  $\Psi$  determines whether the actual OCV is equal to the  $OCV_{charge}$  ( $\Psi = 1$ ), equal to the  $OCV_{discharge}$  ( $\Psi = 0$ ) or lies somewhere in-between ( $0 < \Psi < 1$ ), according to Eq. (4).

$$OCV(SOC, \Psi) = \Psi \cdot OCV_{charge}(SOC) + (1 - \Psi) \cdot OCV_{discharge}(SOC) \quad (4)$$

**Table 1**

Fitted model parameters for OCV hysteresis reconstruction.

| Parameter | Value |
|-----------|-------|
| $k_1$     | 0.332 |
| $k_2$     | 0.668 |
| $m_1$ [%] | 40.1  |
| $m_2$ [%] | 6.3   |

The hysteresis factor can generally be calculated by normalized integration of the charge throughput. We suggest to assess  $\Psi$  using two saturated current integrators, according to Eq. (5) with the normalization factors  $k_1$  and  $k_2$  ( $k_1 + k_2 = 1$ ) and the state values  $\Psi_1$  and  $\Psi_2$ . The state values  $\Psi_1$  and  $\Psi_2$  are limited to a range of 0, ..., 1 each and can be achieved by factorized current integration (Eq. (5)). Therefore, the width factors  $m_1$  and  $m_2$  are introduced, which determine the charge throughput for the transition from  $\Psi_1 = 0$  to  $\Psi_1 = 1$  and  $\Psi_2 = 0 \rightarrow 1$ , respectively. Using two saturated integrators enables the reconstruction of the characteristic hysteresis "eyes".

$$\Psi = k_1 \cdot \Psi_1 + k_2 \cdot \Psi_2 = k_1 \cdot \int \frac{m_1 \cdot I_{cell}}{C_{nom}} dt + k_2 \cdot \int \frac{m_2 \cdot I_{cell}}{C_{nom}} dt \quad (5)$$

Model parameters  $k_1$ ,  $k_2$ ,  $m_1$ , and  $m_2$  are fitted to the measured OCV values, which are achieved from the six partial gradual cycle tests (see Section 3.1), using a least squares parameter fit. The obtained parameter values are given in Table 1.

The reconstructed OCV values are illustrated in Fig. 5, also the measured OCV values from Fig. 4. The obvious curvature of the OCV curves, surrounding the hysteresis "eye", do not result from the hysteresis model itself, they arise from the boundary curves ( $OCV_{charge}$  and  $OCV_{discharge}$ ) included to the model. Even if the demonstrated hysteresis model is very simple, the OCV can be simulated accurately bearing deviations of less than 2 mV throughout all the test cases described in Section 3.1.

Due to the superposition of OCV recovery and OCV hysteresis effects, Eqs. (3) and (4) can be concatenated to one comprehensive equation (Eq. (6)) that determines the cell's OCV depending on the actual SOC, the recovery factor  $\lambda$ , and the hysteresis factor  $\Psi$ .

$$OCV(SOC, \lambda, \Psi) = \Psi \cdot (\lambda \cdot OCV_{1min,charge}(SOC) + (1 - \lambda) \cdot OCV_{3h,charge}(SOC)) + (1 - \Psi) \cdot (\lambda \cdot OCV_{1min,discharge}(SOC) + (1 - \lambda) \cdot OCV_{3h,discharge}(SOC)) \quad (6)$$

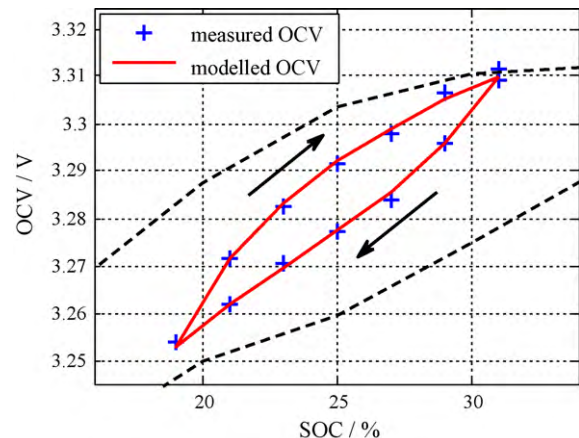


**Fig. 5.** Reconstructed OCV data for the gradual downward test cycle at  $SOC = 25\%$ .

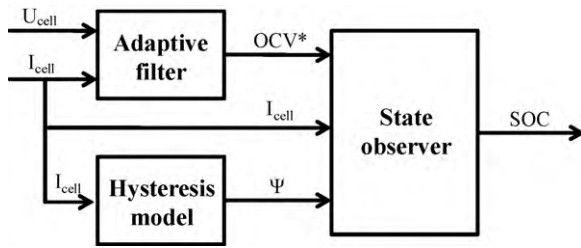


Fig. 6. Schematic illustration of the cascaded state estimation method.

#### 4.3. Validation

With Eqs. (1), (2), (5) and (6) a simple generic battery model is presented, that is easy to parameterize and implement in battery control systems. Using the battery model for state estimation, its ability to simulate battery behavior accurately and its usability in battery control systems can be proved. The intention is to obtain the instantaneous battery's state-of-charge (SOC) information from the measurable values: voltage  $U_{\text{cell}}$  and current  $I_{\text{cell}}$ . Therefore, the battery model is used in a cascaded model-based state estimation function, that is schematically depicted in Fig. 6. This state estimation method includes the presented hysteresis model, an adaptive filter, and a linear state observer term. The distinct model parts are implemented in the Matlab/Simulink development environment and the voltage and current sequences during the NEDC test cycles are used as input data.

The adaptive filter extracts the instantaneous open-circuit-voltage from the actual cell voltage ( $\rightarrow \text{OCV}^*$ ). The filter itself is a two stepped function (for each time step  $k$ ). Firstly, in the prediction step the cell voltage  $\hat{U}_{\text{cell}}$  is calculated with Eq. (7), where  $\underline{\theta}$  is the parameter vector with  $\underline{\theta}_k = [b_{0,k}; b_{1,k}; a_{1,k}; \text{OCV}_k^*]$  and  $\underline{h}_k = [I_{\text{cell},k}; I_{\text{cell},k-1}; (\text{OCV}_{k-1}^* - U_{\text{cell},k-1}); 1]$  is the input vector derived from the input data values. Therefore, Eq. (7) is the time discrete solution of Eq. (1), with the distinct correspondence between the coefficients  $b_0$ ,  $b_1$ ,  $a_1$  and the equivalent circuit components  $R_s$ ,  $R_p$  and  $C_p$ , according to the *Tustin*-transformation [18]. Thereafter, in the correction step the parameter vector coefficients are manipulated by comparing the predicted voltage  $\hat{U}_{\text{cell}}$  to the measured cell voltage  $U_{\text{cell}}$ , according to Eq. (8), where  $K_f$  is the correction gain diagonal matrix. The matrix  $K_f$  has the diagonal elements  $k_{b0}$ ,  $k_{b1}$ ,  $k_{a1}$  and  $k_{\text{OCV}}$ . By adapting the parameter vector  $\underline{\theta}_k$  the prediction error (difference between predicted voltage  $\hat{U}_{\text{cell}}$  and measured voltage  $U_{\text{cell}}$ ) is recursively minimized. From the parameter vector  $\underline{\theta}$  the virtual  $\text{OCV}^*$  is directly accessible and is incorporated in the state observer term.

$$\hat{U}_{\text{cell},k} = \underline{\theta}_{k-1}^T \cdot \underline{h}_k \quad (7)$$

$$\underline{\theta}_k = \underline{\theta}_{k-1} + (U_{\text{cell},k} - \hat{U}_{\text{cell},k}) \cdot K_f \cdot \underline{h}_k \quad (8)$$

The hysteresis model term calculates the hysteresis factor  $\Psi$  referring to Eq. (5), depending on the current sequence. Furthermore, the recovery factor  $\lambda$  is derived with Eq. (2). In order to use the sampled input data (discrete measured values at each time step  $k$  of the cell voltage  $U_{\text{cell},k}$  and current  $I_{\text{cell},k}$ , with the sample time step width  $T$ ) the state equations (Eqs. (2) and (5)) are solved in the time discrete domain.

In the state observer part an SOC is forecasted through normalized current integration with Eq. (9). From the SOC forecast the OCV is calculated with Eq. (6), considering the actual hysteresis and recovery factor ( $\Psi$  and  $\lambda$ ). A difference between the virtual  $\text{OCV}^*$  derived from the cell voltage and OCV derived from current integration leads to an SOC adaptation with Eq. (10), where  $k_B$  is the

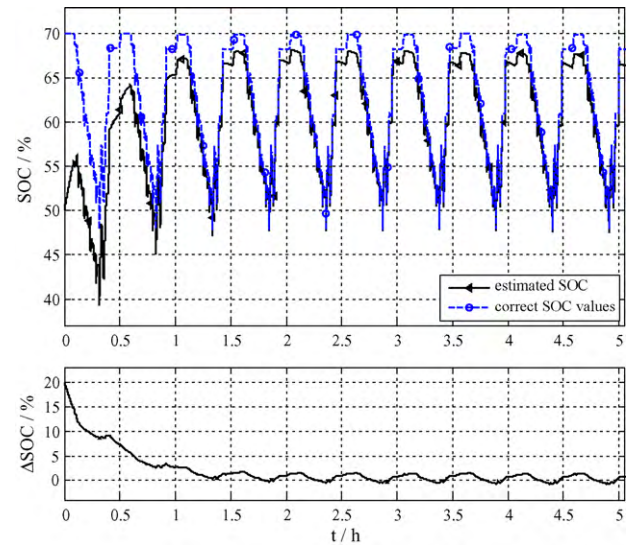


Fig. 7. Estimated and correct SOC sequence during the validation test cycle (top) and the progress of the difference  $\Delta \text{SOC}$  between the both SOC values (bottom).

voltage feedback gain.

$$\text{SOC}_{k|k-1} = \text{SOC}_{k-1} + \frac{I_{\text{cell},k-1} \cdot T}{C_{\text{nom}}} \quad (9)$$

$$\text{SOC}_k = \text{SOC}_{k|k-1} + k_B \cdot (\text{OCV}_k^* - \text{OCV}(\text{SOC}_{k|k-1}, \lambda_k, \Psi_k)) \quad (10)$$

Hence, the cell current as well as the cell voltage is incorporated in the determination of SOC. This special feature of the model-based SOC estimation methods is advantageous in use according to the ability to compensate possible offset errors in the current measurement, which would lead to cumulative errors in the estimated SOC over longer operation periods [19]. An accurate SOC estimation or a recalibration of wrongly initialized SOC is possible only if the battery model operates precisely. This special case of a falsely initialized SOC is investigated with the demonstrated estimation method, incorporating the introduced battery model of the LiFePO<sub>4</sub>-based Li-ion cells. Therefore, an incorrect SOC = 50% is used for initialization before the ten NEDC cycles are applied to the cells successively (correct initial SOC = 70%).

Fig. 7 gives the progress of the instantaneous SOC and the estimated SOC values during the entire validation test, plotted over time.

Recognizably, the estimated SOC starting at SOC = 50% is adapted to the correct SOC during rest and operation periods as well. This is visible in the bottom diagram of Fig. 7, where the decreasing difference between the estimated and the correct SOC is illustrated. After 12 min of operation the SOC failure is less than 10% and after 38 min the failure is less than 5% and thereafter remains in a corridor around  $\Delta \text{SOC} = 0\%$  with an observable jitter of less than 2% (for  $k_B = 0.005$  in the voltage feedback term). This indicates that the demonstrated battery model of the LiFePO<sub>4</sub>-based Li-ion cells is able to reproduce the electric behavior precisely. The model can be implemented in battery management units in order to generate reliable SOC information. The presented model and method works precisely, even if the battery cells comprise very flat OCV curves, superposed by pronounced hysteresis effects and they are operating in the mid SOC range only, without SOC recalibration.

#### 5. Conclusions

This work illustrates the results from investigations on Li-ion cells including cathode active material based on lithium iron phosphate (LiFePO<sub>4</sub>). The obtained results reveal that the cells on one

hand show a typical ohmic-transient behavior under load, that is also known from other battery technologies. This ohmic-transient behavior can easily be reconstructed using a simple electric equivalent circuit. On the other hand side, the open-circuit-voltage characteristics of the cells are very special (i.e. very flat OCV curves with a pronounced hysteresis phenomena superimposed by SOC dependent recovery effects). A battery model of the  $\text{LiFePO}_4$ -based cells is demonstrated, incorporating OCV hysteresis and recovery effects. The battery model is validated by reconstructing the actual battery's voltage during operation very precisely. Therefore, the model can be used for reliable SOC estimation in battery management systems.

## References

- [1] A. Yamada, S.C. Chung, K. Hinokuma, J. Electrochem. Soc. 148 (2001) 224–229.
- [2] J. Shim, A. Guerfi, K. Zaghib, K. Striebel, Effect of Conductive Additives in  $\text{LiFePO}_4$  Cathode for Lithium-ion Batteries, 2003, <http://repositories.cdlib.org/lbnl/LBNL-54101>.
- [3] A. Jossen, W. Weydanz, Moderne Akkumulatoren richtig einsetzen, Inge Reichardt Verlag, 2006, ISBN 3-939359-11-4, <http://www.batteriebuch.de>.
- [4] H. Nakamura, D. Yumoto, Y. Ochi, SICE 2003 Annual Conference, vol. 2, 2003, pp. 2239–2244.
- [5] F. Codeca, S. Savaresi, G. Rizzoni, IEEE International Conference on Control Applications CCA, 2008, pp. 102–107.
- [6] S. Santhanagopalan, R.E. White, J. Power Sources 161 (2006) 1346–1355.
- [7] M. Urbain, S. Rael, B. Davat, P. Desprez, Power Electronics Specialists Conference, PESC 2007 IEEE, 2007, pp. 2804–2810.
- [8] G.L. Plett, J. Power Sources 134 (2004) 252–292.
- [9] G.L. Plett, J. Power Sources 161 (2006) 1356–1384.
- [10] I.-S. Kim, J. Power Sources 163 (2006) 584–590.
- [11] M. Chen, G. Rincon-Mora, IEEE Trans. Energy Convers. 21 (2006) 504–511.
- [12] R.W.J.M. Huang, F. Chung, E.M. Kelder, J. Electrochem. Soc. 153 (2006) A1459–A1465.
- [13] J. Gerschler, D.U. Sauer, EVS 24 (2009).
- [14] V.H. Johnson, J. Power Sources 110 (2002) 321–329.
- [15] N. Meethong, Y.-H. Kao, S. Speakman, Y.-M. Chiang, Pacific Rim Meeting on Electrochemical and Solid-State Science, 2008.
- [16] T. Zheng, J. Dahn, J. Power Sources 68 (1997) 201–203.
- [17] M. Thele, O. Bohlen, D.U. Sauer, E. Karden, J. Power Sources 175 (2008) 635–643.
- [18] H. Unbehauen, Regelungstechnik II—Zustandsregelungen, digitale und nicht-lineare Regelsysteme, Vieweg Verlag, 1985, ISBN 3-528-13348-1.
- [19] R. Portas, L. Colomel, Accuracy of Hall-Effect Current Measurement Transducers in Automotive Battery Management Applications using Current Integration, Automotive Power Electronics, Paris, 2007.